Published in final edited form as:
Cancer Res. 2014 October 1; 74(19): 5397–5408. doi:10.1158/0008-5472.CAN-14-0796.

Sentinel lymph node biopsy revisited: ultrasound-guided photoacoustic detection of micrometastases using molecularly targeted plasmonic nanosensors

Geoffrey P. Luke[1,2], **Jeffrey N. Myers**[3], **Stanislav Y. Emelianov**[1,2,4,*], and **Konstantin V. Sokolov**[2,4,*]

[1]Department of Electrical and Computer Engineering, The University of Texas at Austin, Austin, TX, USA

[2]Department of Biomedical Engineering, The University of Texas at Austin, Austin, TX, USA

[3]Department of Head and Neck Surgery, The University of Texas MD Anderson Cancer Center, Houston, TX, USA

[4]Department of Imaging Physics, The University of Texas MD Anderson Cancer Center, Houston, TX, USA

Abstract

Metastases rather than primary tumors are responsible for killing most cancer patients. Cancer cells often invade regional lymph nodes (LN) before colonizing other parts of the body. However, due to the low sensitivity and specificity of current imaging methods to detect localized nodal spread, an invasive surgical procedure - sentinel lymph node biopsy - is generally employed to identify metastatic cancer cells. Here we introduce a new approach for more sensitive in vivo detection of lymph node micrometastases, based on the use of ultrasound-guided spectroscopic photoacoustic (sPA) imaging of molecularly-activated plasmonic nanosensors (MAPS). Using a metastatic murine model of oral squamous cell carcinoma, we showed that MAPS targeted to the EGFR shifted their optical absorption spectrum to the red-near-infrared region after specific interactions with nodal metastatic cells, enabling their non-invasive detection by sPA. Notably, LN metastases as small as 50 μm were detected at centimeter-depth range with high sensitivity and specificity. Large sPA signals appeared in metastatic LN within 30 minutes of MAPS injection, in support of the clinical utility of this method. Our findings offer a rapid and effective tool to non-invasively identify micrometastases as an alternate to sentinal node biopsy analysis.

Keywords

Photoacoustic imaging; sentinel lymph node; plasmonic nanoparticles; micrometastases; cancer staging; plasmon resonance coupling

---

[*]To whom correspondence should be addressed: Stanislav Emelianov (imaging), 107 W. Dean Keeton St., Austin, TX 78712, USA, 512-471-1733 (phone), 512-471-0616 (fax), emelian@mail.utexas.edu; Konstantin Sokolov (nanosensors), 1515 Holcombe Blvd., Houston, TX 77030, USA, 713-745-0620 (phone), 713-563-2986 (fax), ksokolov@mdanderson.org.

Conflict of Interest: The authors declare no potential conflicts of interest.

Introduction

Accurate detection of regional lymph node (LN) metastases is a critical step in staging, prognosis and development of a treatment plan for cancer patients (1-3). Lymphatic mapping with sentinel lymph node (SLN) biopsy has been introduced as an alternative to elective LN dissection and has gained rapid acceptance because it allows improved accuracy and decreased patient morbidity for regional cancer staging (4, 5). However, SLN biopsy still has major limitations. The procedure requires two or more injections of radionuclide tracers followed by an invasive surgical procedure associated with removal of one or more lymph nodes identified as SLNs with associated risks of short and long term morbidity and up to two weeks of waiting for full histopathology evaluation (6, 7). In addition, the detection limits for pathologic identification of metastatic cells remain subject to the skill and patience of the pathologist. In fact, LN metastases go undetected in up to 9% of melanoma patients, allowing the disease to spread untreated (8). Therefore, there is a definite and urgent clinical need for an imaging technique that is widely available, is noninvasive and simple to perform, is safe, and can reliably detect and adequately diagnose lymph node micrometastases in real-time.

A host of imaging modalities have been tested in animals and patients in attempts to improve the accuracy and safety of SLN biopsy (9-14). For example, ultrasound (US) imaging has been used to detect changes in lymph node size, shape, and blood flow which are associated with metastasis (10). In addition, US imaging of microbubbles and fluorescence imaging of dye have been proposed as an approach to guide SLN biopsy (14, 15). Positron emission tomography (PET) has showed limited sensitivity in detection of metastatic deposits and has been able to reliably detect metastasis only with sizes greater than 80 mm^3 (11). Magnetic resonance imaging (MRI) of systemically injected superparamagnetic iron oxide nanoparticles has been shown to indirectly indicate potential presence of metastasis by detecting a disrupted drainage in metastatic LNs (16). Therefore, although these imaging approaches have shown potential in providing useful morphological and functional information, to date none have demonstrated sufficient sensitivity and specificity to replace the current invasive SLN procedure (11, 12).

Photoacoustic (PA) imaging has recently been introduced as a modality that can improve the detection threshold and sensitivity of radiographic imaging modalities (17-22). It is an emerging hybrid imaging technique that combines the high contrast and sensitivity of optical imaging with the excellent depth resolution of US imaging. Images are acquired by detecting broadband US waves which propagate from sites of optical absorption after the tissue is irradiated with a nanosecond pulsed laser. Previous studies have shown that PA imaging can accurately track intradermally-injected dyes or nanoparticles for localization of LNs with high sensitivity (23, 24). However, even though these approaches eliminate the use of radioactive compounds, they still require surgical removal and histopathological evaluation of the SLNs and they do not provide information about the metastatic state of the SLN.

To address the need for molecular-specific detection of micrometastasis with enhanced specificity and sensitivity, we developed a novel method based on spectroscopic photoacoustic (sPA) imaging with molecularly-activated plasmonic nanosensors (MAPS). The MAPS (Fig. 1a) consisted of 40-nm spherical gold nanoparticles (AuNPs) targeted to the epidermal growth factor receptor (EGFR), a molecular target associated with carcinogenesis in many cancers including lung, oral cavity, and cervix (25), through directional conjugation with anti-EGFR monoclonal antibodies and polyethylene glycol (PEG) (26, 27). Here, we show that MAPS can be used in *in vivo* applications where nonspecific signal due to delivery of a contrast agent hinders the ability to visualize the underlying molecular expressions. In an orthotopic nude mouse model of squamous cell carcinoma of the oral cavity (SCCOC) that develops LN micrometastases (28) we show that a single peritumoral injection of MAPS followed by sPA imaging is sufficient to detect micrometastases as small as 50 μm in size. Molecular-specific interactions between the EGFR-targeted MAPS and tumor cells leads to a dramatic change in the spectroscopic signal of MAPS in sPA imaging that enables highly sensitive detection of micrometastasis. Thus, the combination of traditional US imaging to provide guidance and anatomical information with sPA MAPS-based detection of cancer cells provides an integrated technique for the detection of small micrometastases with high sensitivity and specificity. Our method has a great potential for clinical translation because it is based on a combination of a well-established US imaging and emerging clinically translatable sPA imaging and MAPS. This powerful combination can provide dramatic improvement in the clinical staging, prognosis and therapeutic planning for cancer patients with metastatic disease.

Materials and Methods

Nanoparticle Synthesis

Molecular targeted AuNPs were synthetized as previously described (26). First, 40 nm spherical AuNPs were prepared by heating 100 mL of a 0.01% (w/v) water solution of chloroauric acid ($HAuCl_4$, Sigma-Aldrich) to boiling, and rapidly adding 4 mL of a 1% (w/v) solution of sodium citrate. Then, anti-EGFR or anti-RG16 monoclonal antibodies (clone C225 or RG16, Sigma-Aldrich) were attached to the AuNPs using directional conjugation chemistry that utilizes a carbohydrate chain on the Fc portion of the antibody leaving antigen binding sites on the Fab moiety available for targeting (26). Briefly, antibodies at 1 mg/mL in 40 mM HEPES buffer, pH 7.5 and 100 mM sodium periodate ($NaIO_4$, Sigma-Aldrich) were mixed at 10:1 (v/v) ratio, respectively, and were incubated for 30 minutes in dark at room temperature to oxidize of hydroxyl groups of the carbohydrate chain in the Fc antibody regions. Then, approximately 100 fold molar excess of a heterofunctional hydrazide-polyethylene glycol-dithiol linker (dithiolaromatic-PEG6k-$CONHNH_2$, SensoPath Technologies) was added to the oxidized antibodies for 1 hour. The hydrazide portion of the linker reacts with aldehydes on antibody molecules to form a stable linkage. The antibody-linker complexes were purified using a 100,000 Da molecular weight cutoff centrifugal filter (Millipore). After purification, the modified antibodies were resuspended in 40 mM HEPES (pH 7.4) at concentration of 0.1 mg/mL and were mixed with as prepared AuNPs at 1:10 antibody/nanoparticle (v/v) ratio for 20 minutes at room temperature. During this step a stable bond is formed between the gold surface and the linker's thiol groups. Subsequently, 10^{-5}M 1x phosphate buffered saline (PBS) solution of methoxy-poly(ethylene-glycol)thiol (mPEG-SH, 14 kD, Shearwater Polymers) was added at *ca*. 1:10 mPEG-SH to nanoparticle ratio (v/v) for 20 minutes to passivate the surface of nanoparticle conjugates that is not covered by antibodies (Fig. 1, a). The final conjugates were washed using centrifugation (4000 rpm, 30 minutes) and were resuspended in 1x PBS at concentration of *ca*. 1 × 10^{12} nanoparticles/mL.

Animal Studies

All animal studies were approved by the Institutional Animal Care and Use Committee at The University of Texas at Austin. Balb/c nude mice of 2 months of age were used in this study (Charles River Laboratories). The primary tumors were initiated with a submucosal injection of 300,000 FaDu-Luciferase cells suspended in 30 μL of DMEM media into the tongue. The FaDu cells (ATCC, 2009) are a primary human squamous cell carcinoma of the pharynx cell line which were validated at the Fragment Analysis Facility at Johns Hopkins University via short tandem repeat profiling on January 20, 2011. The cells were passaged for fewer than six months prior to these studies. The tumors were allowed to grow to 3-4 mm in diameter before the imaging experiments were performed. At this point 82% of the inoculated mice developed micrometastases in the cervical LNs.

During US and PA imaging, the mice were anesthetized with isoflurane (1.5%, 0.5 L/min O_2). Heart rate, respiration rate, and body temperature were monitored using a heated electrocardiogram pad. The mice were imaged prior to the injection of nanoparticles. Forty microliters of sterile-filtered nanoparticle solution were injected peritumorally immediately after the first imaging session while the mice were still under anesthesia. The total injected dose was 1.6 pmol of nanoparticles that is equivalent to 40 μg of gold. Imaging was performed continuously for two hours following the injection of nanoparticles.

Following the US and PA imaging, the bioluminescent cancer cells in the mice were imaged using an IVIS Spectrum (PerkinElmer). Once anesthetized with isoflurane, the mice were injected with 100 μL of RediJect D-Luciferin (PerkinElmer). Bioluminescence imaging was performed for 10-15 minutes following the injection. Then mice were euthanized by an overdose of isoflurane and cervical dislocation. Bioluminescence imaging was performed to guide the resection of the primary tumor and metastases. The primary tumor and cervical LNs were fixed in 10% formalin for 24 hours and, then, were transferred to 70% ethanol. Samples were then embedded in paraffin for histological analysis.

Photoacoustic and Ultrasound Imaging

A Vevo LAZR high frequency US and PA imaging system (VisualSonics) equipped with a linear array transducer (LZ-550, 40 MHz center frequency) was used to acquire all PA and US images. The co-registered spatial dimensions of the collected US and PA images were 14 mm (width) by 15 mm (depth). US and PA images at each optical wavelength covering three-dimensional (3-D) volumes surrounding the cervical LNs were acquired by scanning the US transducer in the elevational direction with a step size of 76 μm. The laser was tuned to optical wavelengths of 680, 700, 720, 740, 760, 780, 800, 820, 840, and 860 nm. Laser fluences, measured by a Nova II power meter with a PE50BB sensor (Ophir), were 10-20 mJ/cm^2; all laser energies were below the American National Standards Institute (ANSI) safe exposure level for human skin. Photoacoustic images were averaged 8 times, thus suppressing uncorrelated noise. Each PA image was normalized by the measured fluence to correct for the pulse-to-pulse laser energy variations.

To resolve different types of optical absorbers, we developed an US-guided sPA imaging algorithm. We restricted our analysis to three predominant absorbers: oxygenated hemoglobin (Hb_{O2}), deoxygenated hemoglobin (Hb), and activated MAPS. The US image was used to automatically segment the mouse to remove PA imaging artifacts on the surface of the skin. The relative contributions of Hb_{O2}, Hb, and MAPS to the overall PA signal in each pixel was determined using a previously developed linear least squares method (29). Pixels containing negative concentrations (an artifact arising from noise or the presence of absorbers other than Hb_{O2}, Hb, and MAPS) were not displayed. The oxygen saturation of hemoglobin (SO_2) was computed as the ratio of Hb_{O2} concentration to total hemoglobin concentration. The sPA_{Hb} signal was defined as the total hemoglobin concentration while the sPA_{MAPS} signal was defined as the concentration of activated MAPS. Spectroscopic photoacoustic images were displayed using yellow color for activated sPA_{MAPS} and blue/red colors for sPA_{Hb} with SO_2 varying from 60% (blue) to 100% (red). The range from 100% to 60% was chosen because it represents normal physiological extremes of blood oxygen saturation (e.g., arterial and venous blood). Pixels below 60% SO_2 were colored blue. The intensity of the sPA signal was determined from the average PA signal.

The SLNs were identified and manually segmented using the 3-D visualization of US data. Only the signal inside or within 100 μm of the LNs was considered. The estimated concentrations were filtered with a 5×5×5 voxel median filter to suppress physiological motion. The ratio between the residual of the least squares approximation and the average concentration was used as a threshold to discard pixels whose spectra did not correlate strongly with the analyzed absorbers. In general, most pixels were retained during this operation. We noticed that this step mainly led to a suppression of the signal generated at the surface of the skin (since melanin was not included in spectral analysis). Finally, the total signal stemming from the activated MAPS was summed throughout each node to be used as an indicator of metastasis.

Histology and Optical Imaging

Formalin fixed, paraffin embedded samples were sliced in 100 μm levels. The samples were stained using hematoxylin and eosin stain (H&E) to show tissue morphology, silver stain to detect gold and anti-EGFR rabbit polyclonal antibodies (Sigma HPA018530, St Louis MO) for molecular specific identification of EGFR(+) metastatic cells. A Leica DMI 3000B microscope coupled to a DFC 290 camera was used to record color images.

Dark-field and hyperspectral imaging were performed on a Leica DM 6000 microscope with a 20x objective and xenon lamp. Hyperspectral imaging was carried out with PARISS® system (Lightform, Inc.) attached to the Leica DM 6000 microscope. The system was calibrated using a multi-ion discharge lamp (MIDL) with known emission spectrum. To normalize scattering spectra with the incident lamp spectrum, a spectrum of the excitation xenon lamp was acquired using a Labsphere Spectralon® calibrated scattering substrate.

Statistical Analysis

A Lilliefors test was used to determine that the sPA_{MAPS} signal in the LNs did not follow a normal distribution. A nonparametric Mann-Whitney U test was used to test the null hypothesis that the sPA_{MAPS} signal in metastatic nodes was not significantly greater than the controls. All lymph nodes from mice injected with EGFR-targeted MAPS were used to evaluate the sensitivity and specificity of the imaging technique. A receive operator characteristic (ROC) curve constructed from the sPA_{MAPS} signal was used to determine the threshold for sensitivity and specificity.

Results

Three distinct states can be encountered *in vivo* after injection of MAPS (Fig 1a): 1) cells with no MAPS present at the site of interest, 2) no interactions between cells and delivered MAPS due to the lack of a molecular biomarker of interest, and 3) molecular specific interactions between cells and targeted MAPS. Hyperspectral and dark field optical microscopy of cell cultures simulating these three states (Fig. 1) show that delivery of MAPS increases optical absorption and scattering in the wavelength range near nanoparticle plasmon resonance peak (Fig. 1b and d), while molecular specific interactions between MAPS and EGFR-expressing cancer cells are associated with plasmon resonance coupling, resulting in striking optical changes including red spectral shift in excess of 100 nm and broadening of nanoparticle extinction spectra (Fig. 1b and e). This sensing method is unique among optical activatable imaging agents, which typically rely on enzymatic cleavage for activation and, therefore, are mostly limited to detection of various proteinases (13).

To establish the utility of MAPS *in vivo*, we performed sPA imaging with MAPS for noninvasive detection of micrometastases in the lymphatics of the orthotopic nude mouse model of SCCOC (28). Either EGFR-targeted MAPS or control AuNPs conjugated with a non-specific RG16 monoclonal antibody were injected peritumorally and were allowed to drain to the cervical LNs of tumor-bearing mice. In clinical practice a similar injection of radionuclide tracers is routinely performed to identify the location of LNs; however, it does not allow for the detection of cancer cells. The RG16 antibody acts as a nonspecific control because it targets heavy chains of rabbit IgG/IgM/IgA, which are not present in mouse or FaDu cells. The injected dose was approximately 1.6 pmol, which is significantly less than a dose of AuNPs with any reported cytotoxicity in vivo (30). The cervical LNs, the site of micrometastatic foci in this mouse model (28), were identified using US imaging.

In order to differentiate cancer cells labeled with MAPS from the background, we implemented an image analysis algorithm to spectroscopically resolve the two major contributors to PA signal in our studies- hemoglobin (sPA_{Hb}) and MAPS-labeled cancer cells (sPA_{MAPS}) - in the red-near-infrared (NIR) wavelength region (Fig. 2). The relative contributions of sPA_{Hb}, and sPA_{MAPS} to the overall PA signal were determined via a linear least squares method (29). The SO_2, as calculated by the ratio between the concentration of oxygenated hemoglobin and total hemoglobin, was used to assign a color to the sPA_{Hb} signal. No significant changes in the red-NIR PA signal intensity from LNs were evident in control groups for several hours following injection of MAPS due to low absorption of non-interacting MAPS in this spectral region and no apparent changes in blood flow. In contrast, a strong increase in the PA signal was observed in LNs harboring metastases less than two hours after administration of MAPS (Fig. 2).

Overlaid US and sPA images of cervical LNs (Fig. 3c-e) depicting the anatomy (gray) and contributions from $\mathrm{sPA_{Hb}}$ (blue/red) and $\mathrm{sPA_{MAPS}}$ (yellow) two hours after the peritumoral injection of MAPS show the ability of our method to detect micrometastases in the lymphatics with high spatial resolution. Lymph nodes are identifiable by a dark bean-shaped region in the US images (outlined using white dashed line); the hypoechoic contrast is typical for lymph nodes in US imaging (see an example in Supplementary Fig. 1) (31). The injection of EGFR-targeted MAPS leads to a strong increase in the $\mathrm{sPA_{MAPS}}$ signal from the LNs with micrometastases (Fig. 3c). A three-dimensional reconstruction of the US/sPA images shows the $\mathrm{sPA_{MAPS}}$ signal is constrained to a small region on the edge of the LN (Fig. 3g), which is consistent with the location of metastases observed in this mouse model. Furthermore, there was excellent correlation between the spatial location of the $\mathrm{sPA_{MAPS}}$ signal and the *in situ* bioluminescence signal from metastatic cells (Fig. 4).

Overall, tumor-bearing mice injected with EGFR-targeted MAPS exhibit a statistically significant increase in $\mathrm{sPA_{MAPS}}$ signal from metastatic LNs (N = 7 nodes) over LNs of control mice injected with RG16-conjugated AuNPs (N = 7 nodes, p = 0.006) and either LNs of normal mice (N = 5 nodes) or healthy LNs in tumor-bearing mice (N = 3 nodes) injected with EGFR-targeted MAPS (total N = 8 nodes, p = 0.005; Fig. 3f). Statistical analysis of the data results in a sensitivity of 100% and a specificity of 87.5% of our method in detection of lymph node micrometastasis. The results show that our method is able to detect metastases as small as 50 μm (which was determined by measuring the longest diameter of the metastasis across all histology slices), which corresponds to approximately 30 cells (if we assume a spherical metastasis and cell diameter of 15 μm). The single false-positive came from a LN in a tumor-bearing mouse with a confirmed metastasis in the contralateral cervical LN. Given the fact that bilateral LN metastases developed in a large portion of mice in this study (21% of metastatic mice), it is possible that MAPS are more sensitive than the validation using histology (the current gold standard) and this false-positive represents an occult metastasis.

Continuous sPA imaging of cervical LNs immediately following MAPS injection shows progressive labeling of cancer cells over the course of two hours indicating quick delivery and uptake of the nanoparticles (Fig. 5). A steady increase in $\mathrm{sPA_{MAPS}}$ signal amplitude and volume is seen in a small localized region on the border of the LN. The vasculature that is visible throughout the rest of the image experiences little variation over the same timescale. The contrast generated by MAPS generally tended to plateau after two to three hours. This indicates that the optimal time point to perform imaging occurs in the first few hours after the injection. Furthermore, the two hour timescale is consistent with nanoparticle drainage through the lymphatics observed *in vivo* (32, 33) and cellular uptake of MAPS observed *in vitro* (34). Taken together, these observations provide additional support to the conclusion that the highly localized signal is due to tumor-cell mediated activation of MAPS.

Hematoxylin and eosin (H&E) staining (Fig. 6 a-f) confirmed the presence of the metastases which were indicated by the bioluminescence imaging and were detected by sPA imaging of

MAPS. The metastases had a tendency to form in the subcapsular region of the node near the afferent lymphatic vessel or within the vessel itself. This trend is in excellent correlation with the regions of elevated sPA_{MAPS} and bioluminescence signal (Fig. 3, 4, and 6). Immunohistochemistry confirmed the overexpression of EGFR in the micrometastases (Fig. 6 g-i). Furthermore, hyperspectral dark-field reflectance optical microscopy of the excised tissue slices showed strong labeling of tumor cells and plasmon resonance coupling between MAPS at the location of the micrometastases (Fig. 7). No such signal was observed in the metastatic mice injected with RG16-conjugated AuNPs. These results further indicate that activation of MAPS is specific to EGFR overexpressing cells.

Discussion

Molecular specific imaging of small cellular clusters *in vivo* at substantial depth remains a great challenge in modern biology and medicine (35). Attempts have been made to extend virtually every biomedical imaging modality, including PET (36), MRI (37), US imaging (38, 39), optical imaging (40), and PA imaging (21, 22), to localize molecular expressions *in vivo*. Nevertheless, accurate measurements of molecular expressions in a tissue remain a difficult task. Indeed, it is commonly assumed that the presence of a molecularly-targeted contrast agent correlates to the level of expression of the targeted molecule. What this assumption fails to consider is that delivery of a contrast agent to a site of interest and interaction between the agent and its target are two independent events. Therefore, passive accumulation of a contrast agent in a tissue (e.g., via the enhanced permeability and retention effect in tumors (41)) leads to decreased specificity in molecular sensing (35, 42).

Advanced optical imaging techniques, such as Förster Resonance Energy Transfer (43) or fluorescent imaging using activatable probes (13), are able to provide a much more specific visualization of molecular expressions. However, these methods suffer from low penetration depth (less than one millimeter in the ballistic regime of photon transport) or poor resolution and sensitivity at greater depths (40). Furthermore, fluorescent probes are prone to photobleaching. All of these factors severely limit clinical applicability of optical techniques for molecular detection of diseases, including micrometastases. Photoacoustic imaging addresses these limitations by combining the high contrast of optical imaging with the excellent resolution of US imaging at depths up to 5 cm (20-22, 44). In addition, plasmonic nanoparticles characterized by enhanced optical absorption and photostability provide strong contrast in PA imaging (19, 44, 45). However, previous efforts to combine plasmonic nanoparticles with *in vivo* PA imaging have not addressed the fundamental challenge in specificity that most other molecular imaging modalities suffer from: nanoparticles which have interacted with a molecule of interest cannot be differentiated from those which have simply been delivered to the region.

Our approach based on nano-scale interactions between cells and MAPS provides a straightforward mechanism to decouple nanoparticle delivery from molecular interactions (Supplementary Fig. 2). Our results show an excellent ability to detect small colonies of cancerous cells. Indeed, the 100% sensitivity and 87.5% specificity of sPA imaging of MAPS are significantly better than the results obtained using other non-invasive imaging modalities (46). For example PET, while more sensitive than many other radiographic modalities, has 50% sensitivity and 87% specificity in detection of impalpable cervical metastases in human oral cancer patients (47). Demonstrated here is the capacity to detect metastatic tumors consisting of just few tens of malignant cells deep inside tissue.

The translation of this technique to the clinic will require both a clinical imaging system and a clinically approved contrast agent. The clinical imaging system must be developed to image tissues at 3-5 cm depth. This could be achieved by combining a clinically relevant lower frequency US transducer (e.g., 10 MHz center frequency) with a tunable laser source in the red-NIR spectral region that provides sufficient pulse power at clinically save irradiation levels; this combination will achieve light penetration in tissue and propagation of acoustic waves that are appropriate for lymph node imaging in multiple anatomical locations including lymph nodes associated with oral and breast cancers. In general, we do not expect the approach to depend on the location of the primary tumor or its proximity to the SLN. What is important is that the primary tumor needs to be accessible for an injection of the MAPS and the LNs must be accessible for PA imaging (i.e., they must be within a few centimeters of a handheld or endoscopic imaging probe). We expect that the sensitivity of our imaging method in the clinic will be primarily limited by the ability to deliver light deep in tissue. In addition, while the dose of gold used in this study is well below any previously reported toxicity threshold (30), gold nanoparticles are not yet accepted for widespread clinical use. One of the concerns associated with gold nanoparticles is potential long term toxicity because particles larger than 5-6 nm are not easily cleared from the body. Previous studies have shown that nanoparticles with sizes below *ca*. 6 nm can undergo efficient clearance through urine and feces (48-50). Therefore, scaling down the MAPS to 5 nm is a viable path toward clinical acceptance. Because the MAPS are delivered through the lymphatics, the short half-life of small particles in the bloodstream will not impact our technology as opposed to applications requiring systemic delivery where small particles can undergo quick renal clearance. Overall, the clinical translation of the developed method is possible and anticipated.

Supplementary Material

Refer to Web version on PubMed Central for supplementary material.

Acknowledgments

The work was supported in part by grants from National Institutes of Health (NIH) R01EB008101 and F31CA168168. We would like to thank Dr. Aristarchos Papagiannaros of the University of Texas M.D. Anderson Cancer Center for his help with nanoparticle conjugation, tumor inoculation, and histology in preliminary studies, Dr. Pratixa Joshi, Dr. Justina Tam, and Mr. Chun-Hsien Wu of The University of Texas at Austin for their assistance with nanosphere synthesis and antibody conjugation, Dr. Timothy Larson at The University of Texas at Austin for his help with optical microscopy and hyperspectral image processing of cell cultures, Ms. Sally Amen of the University of Texas at Austin for consulting on the statistical analysis, and Mrs. Nancy Wick Otto of the UT M.D. Anderson Cancer Center Science Park for her expertise on immunohistochemistry optimization and processing.

Funding: This work was funded by NIH grants R01EB008101 and F31CA168168.

References

1. Gershenwald JE, Thompson W, Mansfield PF, Lee JE, Colome MI, Tseng Ch, et al. Multi-Institutional Melanoma Lymphatic Mapping Experience: The Prognostic Value of Sentinel Lymph Node Status in 612 Stage I or II Melanoma Patients. Journal of Clinical Oncology. 1999; 17:976. [PubMed: 10071292]
2. Stoeckli SJ, Steinert H, Pfaltz M, Schmid S. Sentinel Lymph Node Evaluation in Squamous Cell Carcinoma of the Head and Neck. Otolaryngology -- Head and Neck Surgery. 2001; 125:221–6. [PubMed: 11555757]
3. Veronesi U, Paganelli G, Galimberti V, Viale G, Zurrida S, Bedoni M, et al. Sentinel-node biopsy to avoid axillary dissection in breast cancer with clinically negative lymph-nodes. Lancet. 1997; 349:1864–7. [PubMed: 9217757]
4. Bergkvist L, Frisell J. Multicentre validation study of sentinel node biopsy for staging in breast cancer. British Journal of Surgery. 2005; 92:1221–4. [PubMed: 15988791]
5. Ronka R, Smitten K, Sintonen H, Kotomaki T, Krogerus L, Leppanen E, et al. The impact of sentinel node biopsy and axillary staging strategy on hospital costs. Annals of oncology : official journal of the European Society for Medical Oncology / ESMO. 2004; 15:88–94. [PubMed: 14679125]
6. Goldberg J, Riedel E, Morrow M, Van Zee K. Morbidity of Sentinel Node Biopsy: Relationship Between Number of Excised Lymph Nodes and Patient Perceptions of Lymphedema. Annals of Surgical Oncology. 2011; 18:2866–72. [PubMed: 21465310]
7. Langer I, Guller U, Berclaz G, Koechli OR, Schaer G, Fehr MK, et al. Morbidity of Sentinel Lymph Node Biopsy (SLN) Alone Versus SLN and Completion Axillary Lymph Node Dissection After Breast Cancer Surgery: A Prospective Swiss Multicenter Study on 659 Patients. Annals of Surgery. 2007; 245:452–61. [PubMed: 17435553]
8. Scoggins CR, Martin RC, Ross MI, Edwards MJ, Reintgen DS, Urist MM, et al. Factors associated with false-negative sentinel lymph node biopsy in melanoma patients. Annals of surgical oncology. 2010; 17:709–17. [PubMed: 19967459]
9. Cohen SM, Fishinghawk BG, Cohen MS. Translational imaging of lymphatics in cancer. Advanced Drug Delivery Reviews. 2011; 63:956–62. [PubMed: 21683745]
10. Wunderbaldinger P. Problems and prospects of modern lymph node imaging. European Journal of Radiology. 2006; 58:325–37. [PubMed: 16464553]
11. Wagner JD, Schauwecker DS, Davidson D, Wenck S, Jung SH, Hutchins G. FDG-PET sensitivity for melanoma lymph node metastases is dependent on tumor volume. Journal of surgical oncology. 2001; 77:237–42. [PubMed: 11473371]
12. Van der Hoeven JJM, Hoekstra OS, Comans EFI, et al. Determinants of diagnostic performance of [F-18]Fluorodeoxyglucose positron emission tomography for axillary staging in breast cancer. Ann Surg. 2002; 236:619–24. [PubMed: 12409668]
13. Savariar EN, Felsen CN, Nashi N, Jiang T, Ellies LG, Steinbach P, et al. Real-time In Vivo Molecular Detection of Primary Tumors and Metastases with Ratiometric Activatable Cell-Penetrating Peptides. Cancer research. 2013; 73:855–64. [PubMed: 23188503]
14. Kim S, Lim YT, Soltesz EG, De Grand AM, Lee J, Nakayama A, et al. Near-infrared fluorescent type II quantum dots for sentinel lymph node mapping. Nat Biotechnol. 2004; 22:93–7. [PubMed: 14661026]
15. Goldberg BB, Merton DA, Liu JB, Thakur M, Murphy GF, Needleman L, et al. Sentinel Lymph Nodes in a Swine Model with Melanoma: Contrast-enhanced Lymphatic US1. Radiology. 2004; 230:727–34. [PubMed: 14990839]
16. Harisinghani MG, Barentsz J, Hahn PF, Deserno WM, Tabatabaei S, van de Kaa CH, et al. Noninvasive detection of clinically occult lymph-node metastases in prostate cancer. New England Journal of Medicine. 2003; 348:2491–9. [PubMed: 12815134]
17. Zhang HF, Maslov K, Stoica G, Wang LV. Functional photoacoustic microscopy for high-resolution and noninvasive in vivo imaging. Nat Biotech. 2006; 24:848–51.

18. Eghtedari M, Oraevsky A, Copland JA, Kotov NA, Conjusteau A, Motamedi M. High sensitivity of in vivo detection of gold nanorods using a laser optoacoustic imaging system. Nano Lett. 2007; 7:1914–8. [PubMed: 17570730]
19. Luke GP, Yeager D, Emelianov SY. Biomedical applications of photoacoustic imaging with exogenous contrast agents. Ann Biomed Eng. 2012; 40:422–37. [PubMed: 22048668]
20. Diebold GJ, Khan MI, Park SM. Photoacoustic “signatures” of particulate matter: optical production of acoustic monopole radiation. Science. 1990; 250:101–4. [PubMed: 17808241]
21. Wang LV, Hu S. Photoacoustic tomography: in vivo imaging from organelles to organs. Science. 2012; 335:1458–62. [PubMed: 22442475]
22. Beard P. Biomedical photoacoustic imaging. Interface Focus. 2011; 1:602–31. [PubMed: 22866233]
23. Song KH, Stein EW, Margenthaler JA, Wang LV. Noninvasive photoacoustic identification of sentinel lymph nodes containing methylene blue in vivo in a rat model. Journal of Biomedical Optics. 2008; 13:054033–6. [PubMed: 19021413]
24. Song KH, Kim C, Cobley CM, Xia Y, Wang LV. Near-Infrared Gold Nanocages as a New Class of Tracers for Photoacoustic Sentinel Lymph Node Mapping on a Rat Model. Nano Letters. 2008; 9:183–8. [PubMed: 19072058]
25. Barnes CJ, Kumar R. Biology of the epidermal growth factor receptor family. Cancer Treat Res. 2004; 119:1–13. [PubMed: 15164870]
26. Kumar S, Aaron J, Sokolov K. Directional conjugation of antibodies to nanoparticles for synthesis of multiplexed optical contrast agents with both delivery and targeting moieties. Nature Protocols. 2008; 3:314–20.
27. Niidome T, Yamagata M, Okamoto Y, Akiyama Y, Takahashi H, Kawano T, et al. PEG-modified gold nanorods with a stealth character for in vivo applications. Journal of Controlled Release. 2006; 114:343–7. [PubMed: 16876898]
28. Myers JN, Holsinger FC, Jasser SA, Bekele BN, Fidler IJ. An Orthotopic Nude Mouse Model of Oral Tongue Squamous Cell Carcinoma. Clinical Cancer Research. 2002; 8:293–8. [PubMed: 11801572]
29. Kim S, Chen YS, Luke GP, Emelianov SY. In vivo three-dimensional spectroscopic photoacoustic imaging for monitoring nanoparticle delivery. Biomed Opt Express. 2011; 2:2540–50. [PubMed: 21991546]
30. Khlebtsov N, Dykman L. Biodistribution and toxicity of engineered gold nanoparticles: a review of in vitro and in vivo studies. Chemical Society Reviews. 2011; 40:1647–71. [PubMed: 21082078]
31. Richards PS, Peacock TE. The role of ultrasound in the detection of cervical lymph node metastases in clinically N0 squamous cell carcinoma of the head and neck. Cancer Imaging. 2007; 7:167–78. [PubMed: 18055290]
32. Cai X, Li W, Kim CH, Yuan Y, Wang LV, Xia Y. In vivo quantitative evaluation of the transport kinetics of gold nanocages in a lymphatic system by noninvasive photoacoustic tomography. ACS Nano. 2011; 5:9658–67. [PubMed: 22054348]
33. Luke GP, Bashyam A, Homan KA, Makhija S, Chen YS, Emelianov SY. Silica-coated gold nanoplates as stable photoacoustic contrast agents for sentinel lymph node imaging. Nanotechnology. 2013; 24:455101. [PubMed: 24121616]
34. Aaron J, Travis K, Harrison N, Sokolov K. Dynamic imaging of molecular assemblies in live cells based on nanoparticle plasmon resonance coupling. Nano Lett. 2009; 9:3612–8. [PubMed: 19645464]
35. Weissleder R. Molecular imaging in cancer. Science. 2006; 312:1168–71. [PubMed: 16728630]
36. Gambhir SS. Molecular imaging of cancer with positron emission tomography. Nat Rev Cancer. 2002; 2:683–93. [PubMed: 12209157]
37. Lee JH, Huh YM, Jun Yw, Seo Jw, Jang Jt, Song HT, et al. Artificially engineered magnetic nanoparticles for ultra-sensitive molecular imaging. Nature medicine. 2006; 13:95–9.
38. Kaufmann BA, Lindner JR. Molecular imaging with targeted contrast ultrasound. Current opinion in biotechnology. 2007; 18:11–6. [PubMed: 17241779]
39. Foster FS, Pavlin CJ, Harasiewicz KA, Christopher DA, Turnbull DH. Advances in ultrasound biomicroscopy. Ultrasound in medicine & biology. 2000; 26:1–27. [PubMed: 10687788]

40. Weissleder R, Ntziachristos V. Shedding light onto live molecular targets. Nature medicine. 2003; 9:123–8.

41. Maeda H. The enhanced permeability and retention (EPR) effect in tumor vasculature : The key role of tumor-selective macromolecular drug targeting. Adv Enzyme Regul. 2001; 41:189–207. [PubMed: 11384745]

42. Massoud TF, Gambhir SS. Molecular imaging in living subjects: seeing fundamental biological processes in a new light. Genes & development. 2003; 17:545–80. [PubMed: 12629038]

43. Jares-Erijman EA, Jovin TM. FRET imaging. Nature biotechnology. 2003; 21:1387–95.

44. Emelianov SY, Li PC, O'Donnell M. Photoacoustics for molecular imaging and therapy. Physics Today. 2008:34–9.

45. Jain PK, Lee KS, El-Sayed IH, El-Sayed MA. Calculated Absorption and Scattering Properties of Gold Nanoparticles of Different Size, Shape, and Composition: Applications in Biological Imaging and Biomedicine. The Journal of Physical Chemistry B. 2006; 110:7238–48. [PubMed: 16599493]

46. Stuckensen T, Kovács AF, Adams S, Baum RP. Staging of the neck in patients with oral cavity squamous cell carcinomas: a prospective comparison of PET, ultrasound, CT and MRI. Journal of Cranio-Maxillofacial Surgery. 2000; 28:319–24. [PubMed: 11465137]

47. Kyzas PA, Evangelou E, Denaxa-Kyza D, Ioannidis JP. 18F-fluorodeoxyglucose positron emission tomography to evaluate cervical node metastases in patients with head and neck squamous cell carcinoma: a meta-analysis. Journal of the National Cancer Institute. 2008; 100:712–20. [PubMed: 18477804]

48. Choi HS, Liu W, Misra P, Tanaka E, Zimmer JP, Ipe BI, et al. Renal clearance of quantum dots. Nature biotechnology. 2007; 25:1165–70.

49. Schipper ML, Iyer G, Koh AL, Cheng Z, Ebenstein Y, Aharoni A, et al. Particle size, surface coating, and PEGylation influence the biodistribution of quantum dots in living mice. Small. 2009; 5:126–34. [PubMed: 19051182]

50. Park JH, Gu L, Von Maltzahn G, Ruoslahti E, Bhatia SN, Sailor MJ. Biodegradable luminescent porous silicon nanoparticles for in vivo applications. Nature materials. 2009; 8:331–6.

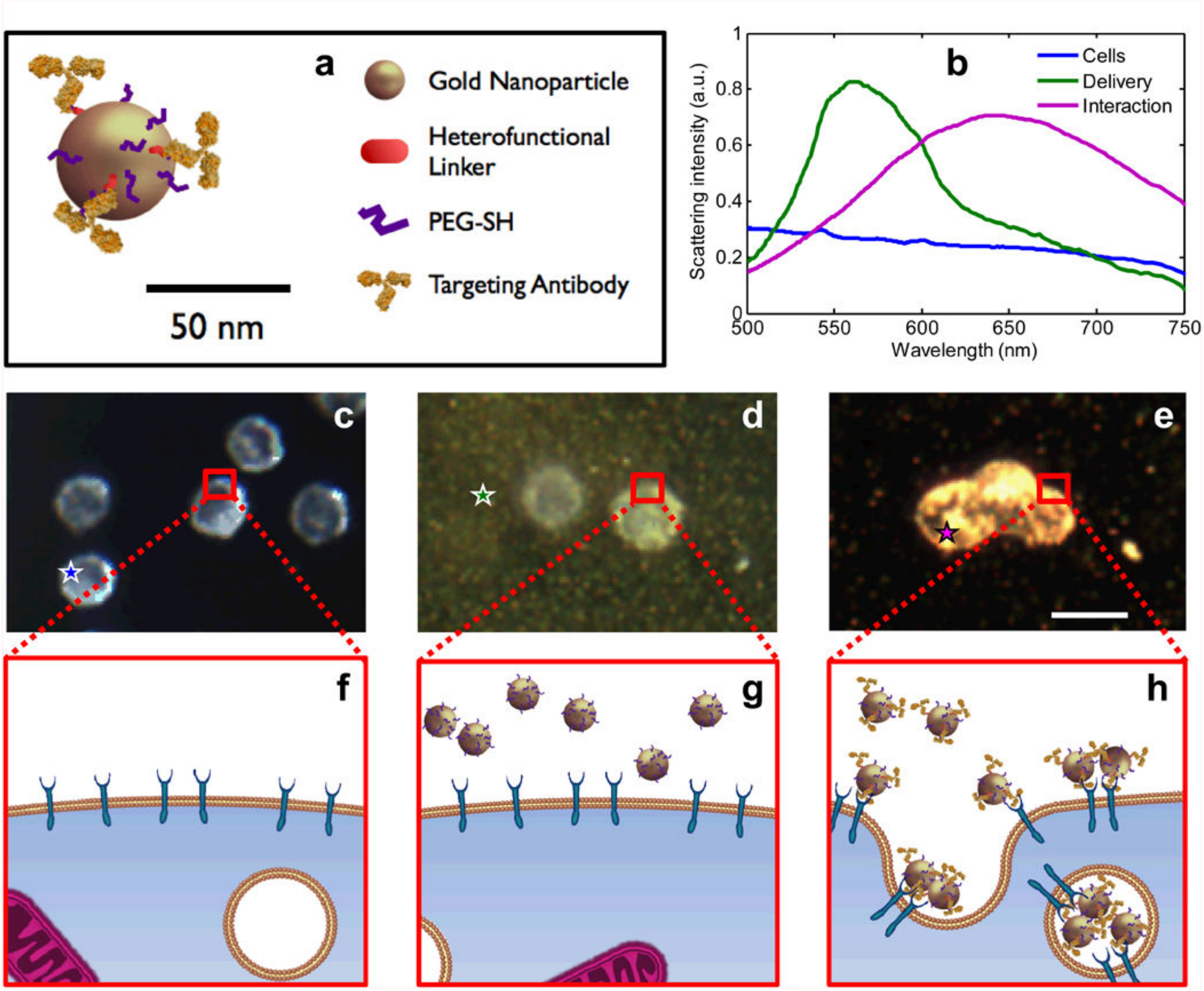

Fig. 1.

The effect of plasmon resonance coupling in molecular specific imaging of EGFR expressing cancer cells. (**a**) A schematic of the EGFR-targeted MAPS; relative dimensions of antibody molecules and a gold nanoparticle (AuNPs) are preserved. (**b**) Hyperspectral darkfield microscopy was used to obtain optical spectra from unlabeled cells (blue), MAPS dispersed in extracellular space (green), and cells labeled with MAPS (violet). Dark-field optical images (**c, d**, and **e**; scale bar is 10 μm) and cartoon (**f, g**, and **h**) show: (**c** and **f**) cancer cells in the absence of gold nanoparticles; (**d** and **g**) cells in the presence of non-specific AuNPs; and (**e** and **h**) cells labeled with MAPS. Unlabeled cells have a characteristic bluish white appearance due to intrinsic light scattering properties (**c**) while a greenish haze is evident in the presence of non-specific AuNPs which strongly scatter green light (**d**). Molecular specific interactions between MAPS and EGFR-overexpressing cancer cells lead to receptor-mediated endocytosis which results in plasmon resonance coupling between MAPS and the associated strong changes in their optical properties (**e**). The colored stars in (**c-e**) identify the regions from which the same-color spectral curves are displayed in (**b**).

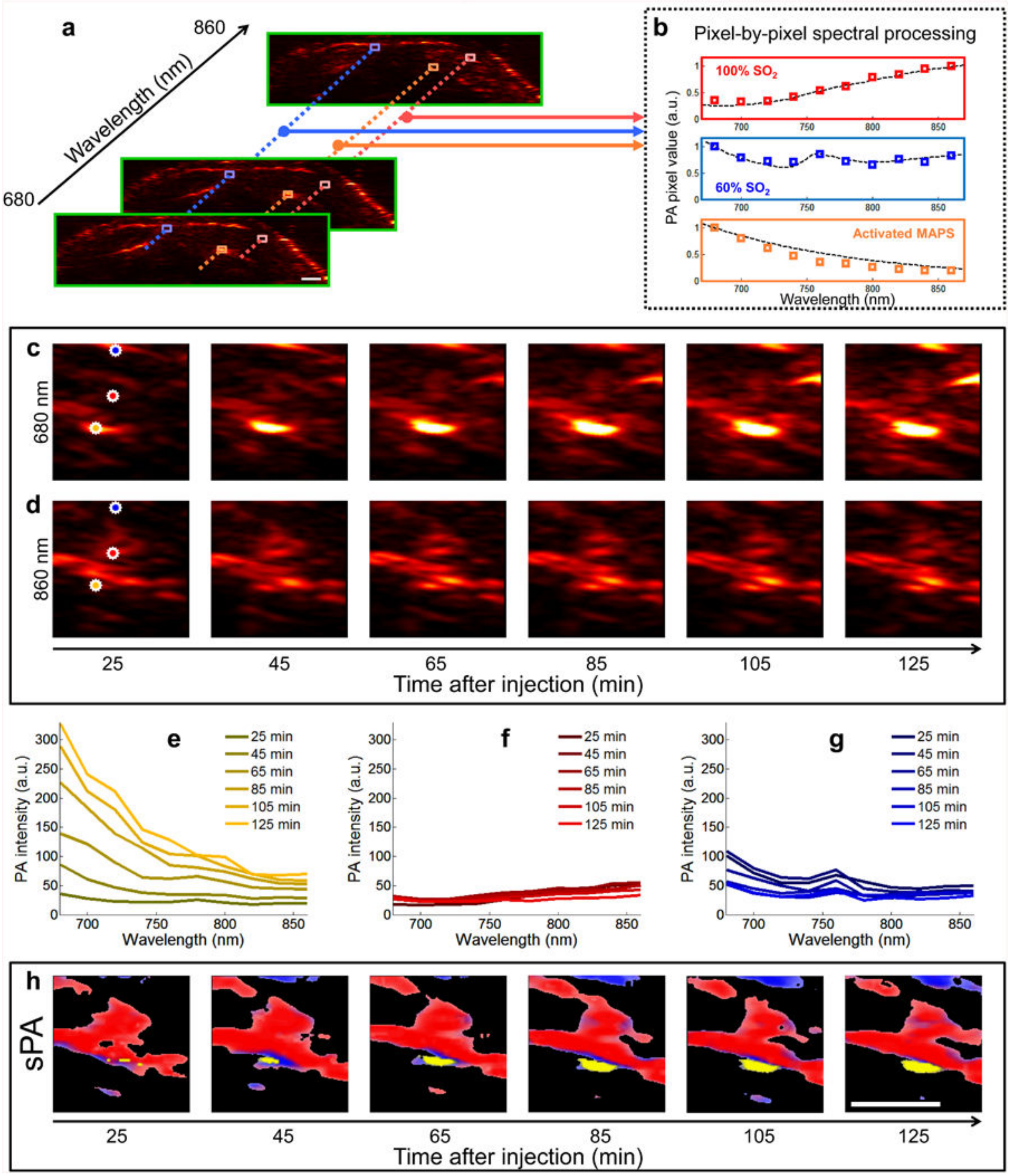

Fig. 2.

Generation of sPA images. (**a**) In each two-dimensional plane PA images are acquired using excitation wavelengths spanning 680 nm to 860 nm in steps of 20 nm. (**b**) Each pixel is compared to hemoglobin and activated MAPS; the dashed lines represent the expected spectra, while the colored boxes are representative measured PA signals. Spectral unmixing is performed using a least squares method (29). An example of spectral unmixing of a series of PA images is shown in (**c-h**). Photoacoustic images acquired at (**c**) 680 nm and (**d**) 860 nm show the raw of PA signal. (**e-g**) The spectra derived from three pixels (denoted by orange, red, and blue stars, for (**e**), (**g**), and (**g**), respectively) of the PA images acquired at 10 wavelengths, including the images from (**c**) and (**d**), exhibit distinct spectral signatures which correlate well with the spectra of hemoglobin or MAPS. The pixel containing signal correlating to the MAPS spectrum steadily increases in amplitude over time (**e**), while the signals corresponding to blood remain relatively constant (**f** and **g**). (**h**) After spectral unmixing, the different absorbers are clearly distinguished as either blood (red/blue) or activated MAPS (yellow). Scale bars are 1 mm.

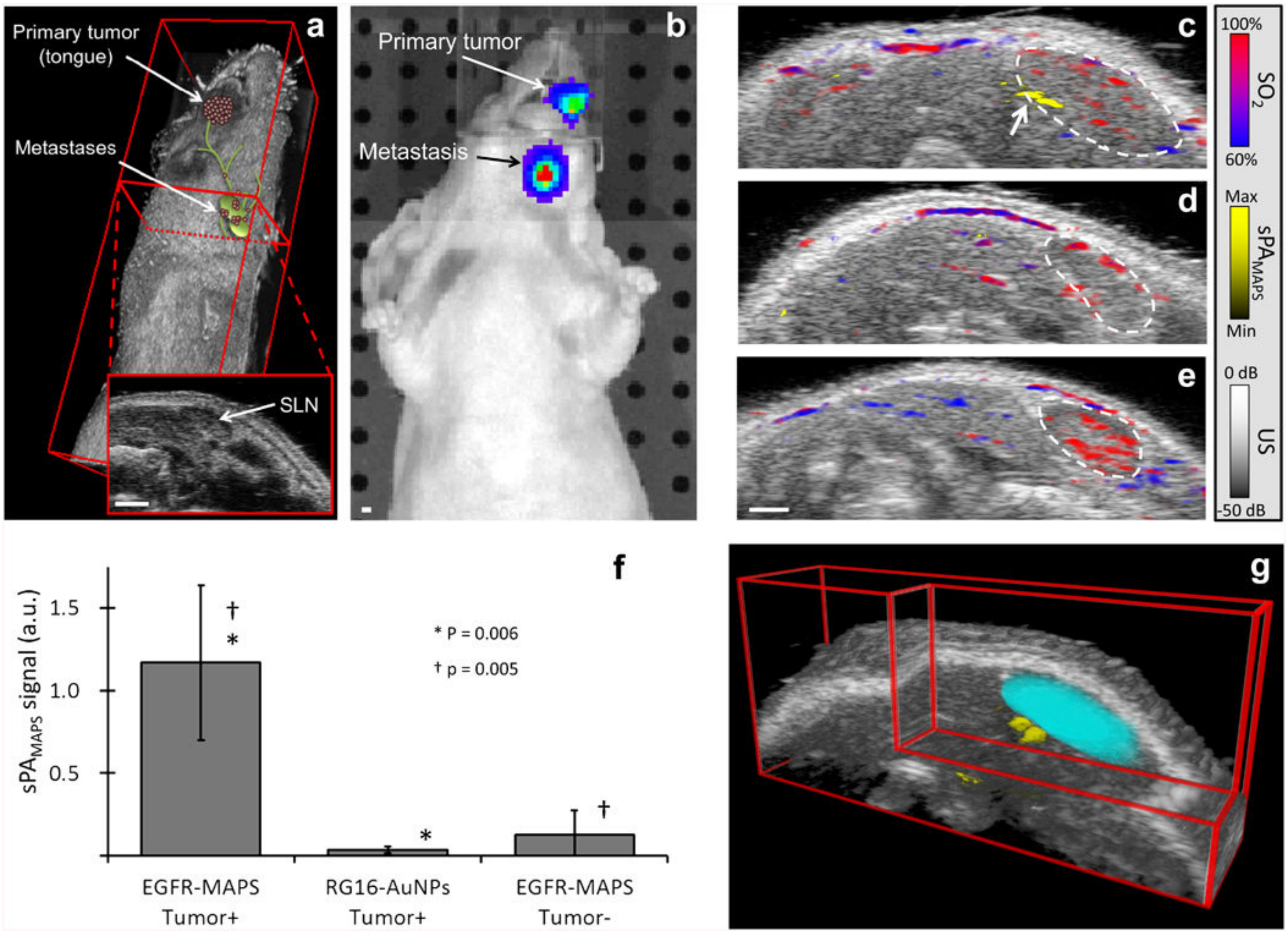

Fig. 3.

In vivo imaging of lymph node micrometastases. (**a**) Three-dimensional US image of a mouse with an overlaid cartoon of the primary tumor in the tongue and micrometastases in the cervical lymph nodes. The inset shows a two-dimensional cross section of the US image with a lymph node seen as the dark, hypoechoic bean-shaped region. (**b**) A representative bioluminescence image confirms the presence of FaDu cells in the primary tumor and in the lymphatic system. Representative overlaid US and sPA images of: a tumor-bearing mouse with a lymph node metastasis two hours after a peritumoral injection of either (**c**) EGFR-targeted MAPS or (**d**) control RG16-conjugated AuNPs and (**e**) a normal mouse two hours after a submucosal injection of EGFR-targeted MAPS. Hemoglobin (sPA_{Hb}) is depicted in red-blue, as determined by the oxygen saturation, while the presence of cancer cells labeled with MAPS (sPA_{MAPS}) is depicted in yellow (see an arrow pointing to a micrometastasis in (c)); the anatomical location of a cervical lymph node is outlined by a dashed white line. Note the strong sPA_{MAPS} signal in tumor-bearing mice injected with EGFR-targeted MAPS. (**f**) The LNs were split into three categories for analysis: 1) LNs containing metastases in mice injected with EGFR-targeted MAPS (N = 7), 2) LNs in tumor bearing mice injected with RG16-conjugated AuNPs (N = 7), and 3) LNs without metastasis in mice with or without a primary tumor injected with EGFR-targeted MAPS (N = 8). The total signal of activated MAPS was used as indictor of metastases. The metastatic lymph nodes in tumor-bearing mice exhibit a statistically significant increase in the sPA_{MAPS} signal. The p values are from a Mann-Whitney U test and error bars correspond to one standard deviation. (**g**) A three-dimensional reconstruction of the US images with the SLN volume segmented from the two-dimensional US images (cyan) with the overlaid three-dimensional sPA image showing the volumetric distribution of the sPA_{MAPS} signal. All scale bars are 1 mm.

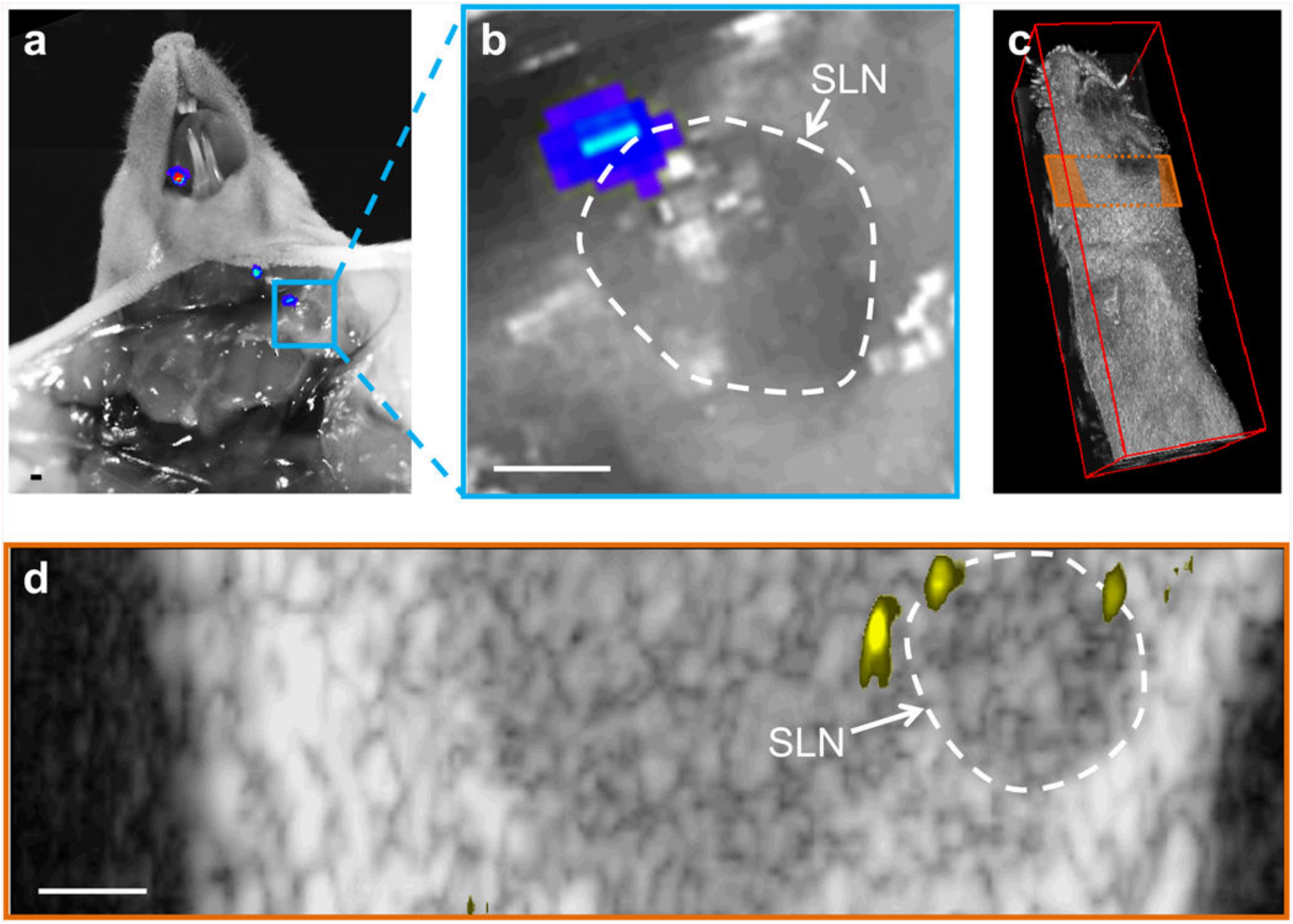

Fig. 4.

Spatial correlation between sPA$_{MAPS}$ signal and bioluminescence. (**a, b**) Photograph with overlaid bioluminescence image showing a small metastasis at the edge of the lymph node. (**c**) Ultrasound image showing the imaging plane depicted in (**d**). (**e**) An ultrasound image of the plane depicted in (**d**) and overlaid sPA$_{MAPS}$ signal shows two micrometastases which generated the bioluminescence signal and a third which was undetected by bioluminescence.

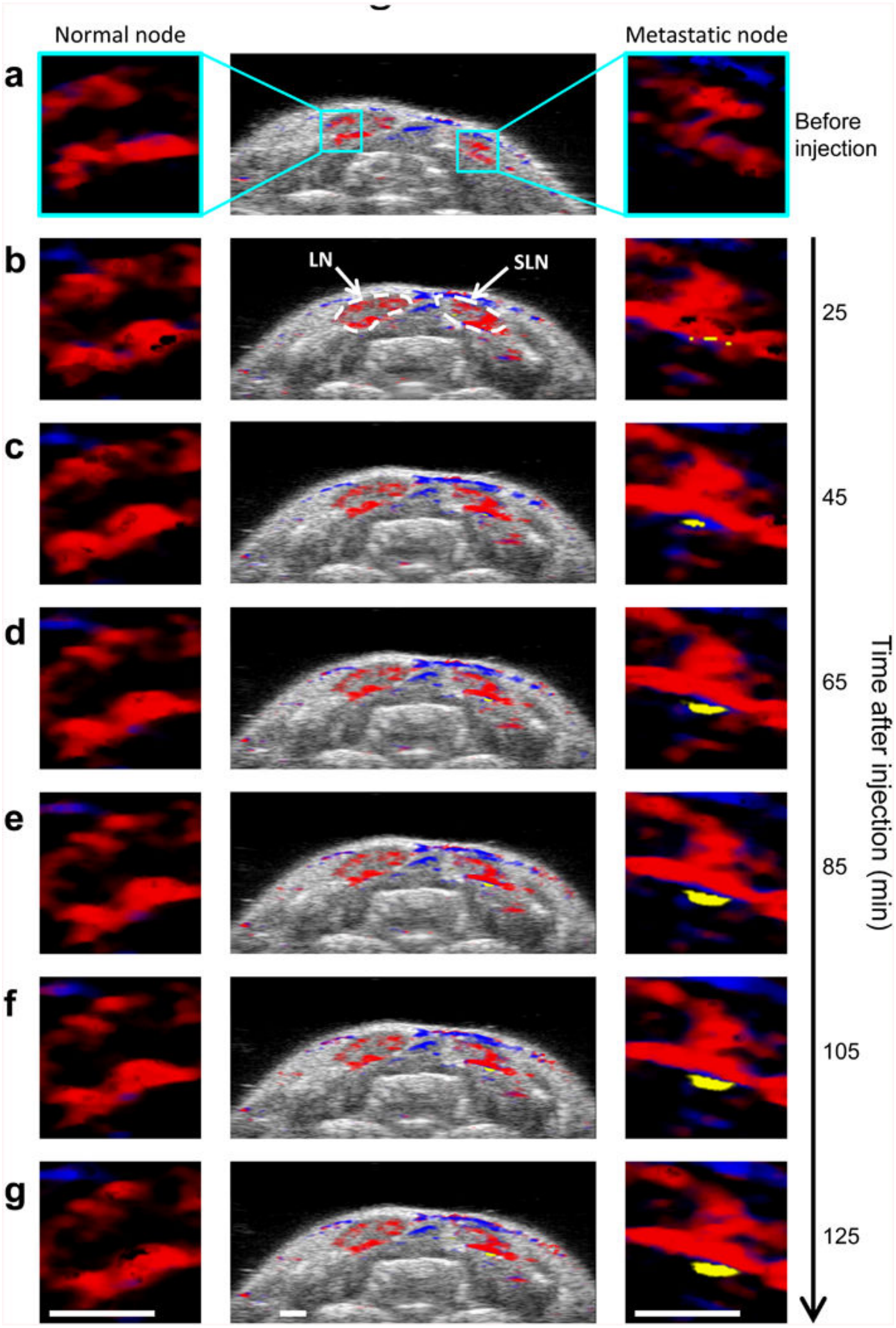

Fig. 5.

Kinetics of MAPS interaction with micrometastasis. Combined US and sPA image of a two-dimensional cross section containing two lymph nodes (center), and 4x enlarged sPA images of a region on the border of the left lymph node (left) and right lymph node (right) (**a**) before, (**b**) 25, (**c**) 45, (**d**) 65, (**e**) 85, (**f**) 105, and (**g**) 125 minutes after the injection of MAPS. The steadily growing region of activated MAPS in the right lymph node indicates that MAPS are gradually being delivered to and are interacting with cancer cells on the border of the lymph node. Scale bars are 1 mm.

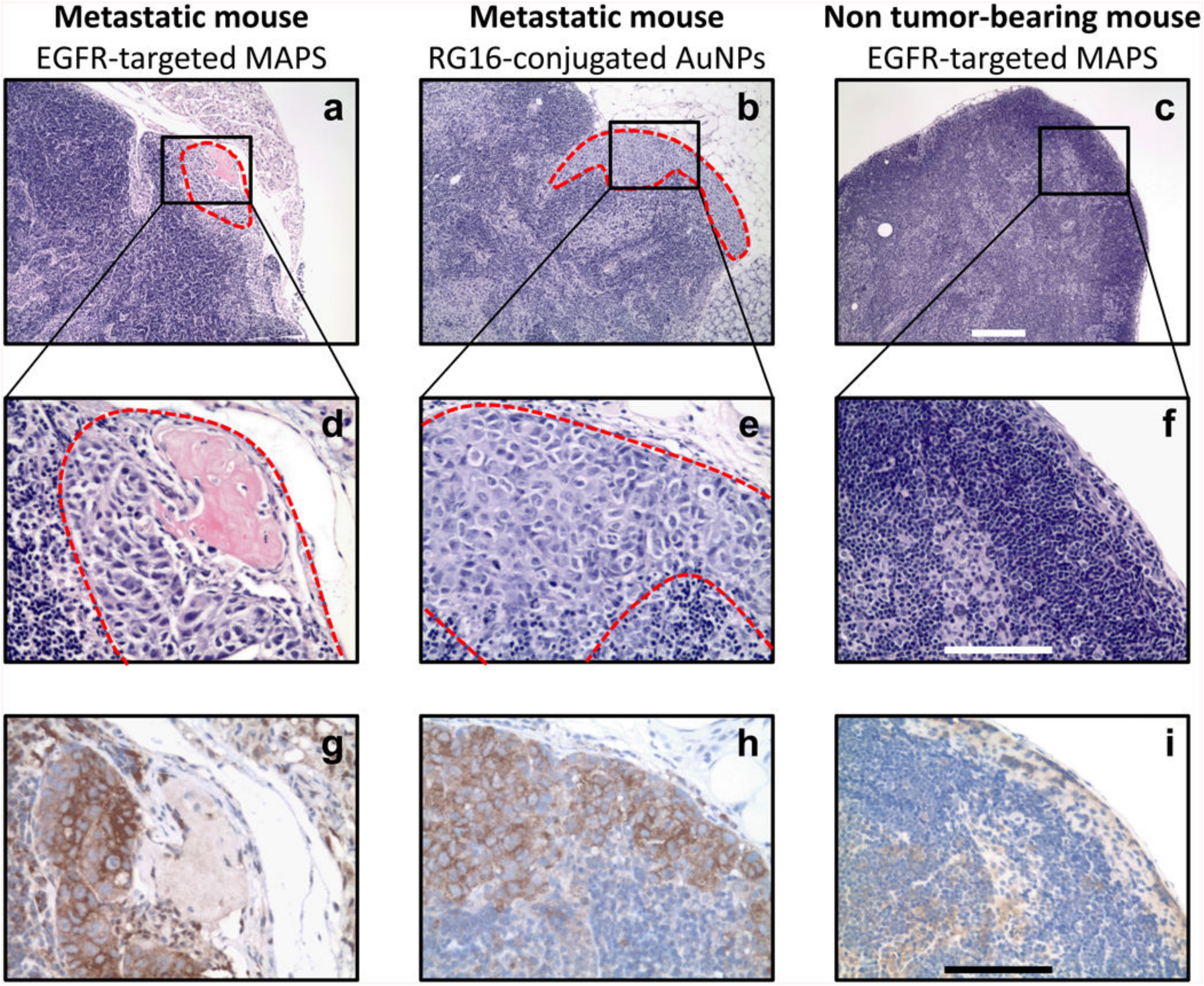

Fig. 6.

Histological evaluation of excised lymph nodes. (**a, b**) H&E staining of lymph nodes from mice with positive bioluminescent signal in lymph nodes shows the subcapsular formation of micrometastases (dashed red outline) near an afferent lymph vessel. (**c**) The morphology of a lymph node from a normal mouse is shown for reference. (**d, e**) At high magnification, the irregular shape and large nuclei indicate presence of cancer cells in H&E sections. (**f**) A normal population of lymphatic cells is seen in normal mice. Immunohistochemical staining shows (**g, h**) elevated expression of EGFR in the micrometastases and (**i**) negligible EGFR expression in normal nodes. Scale bars are 200 µm (a-c) and 100 µm (d-i).

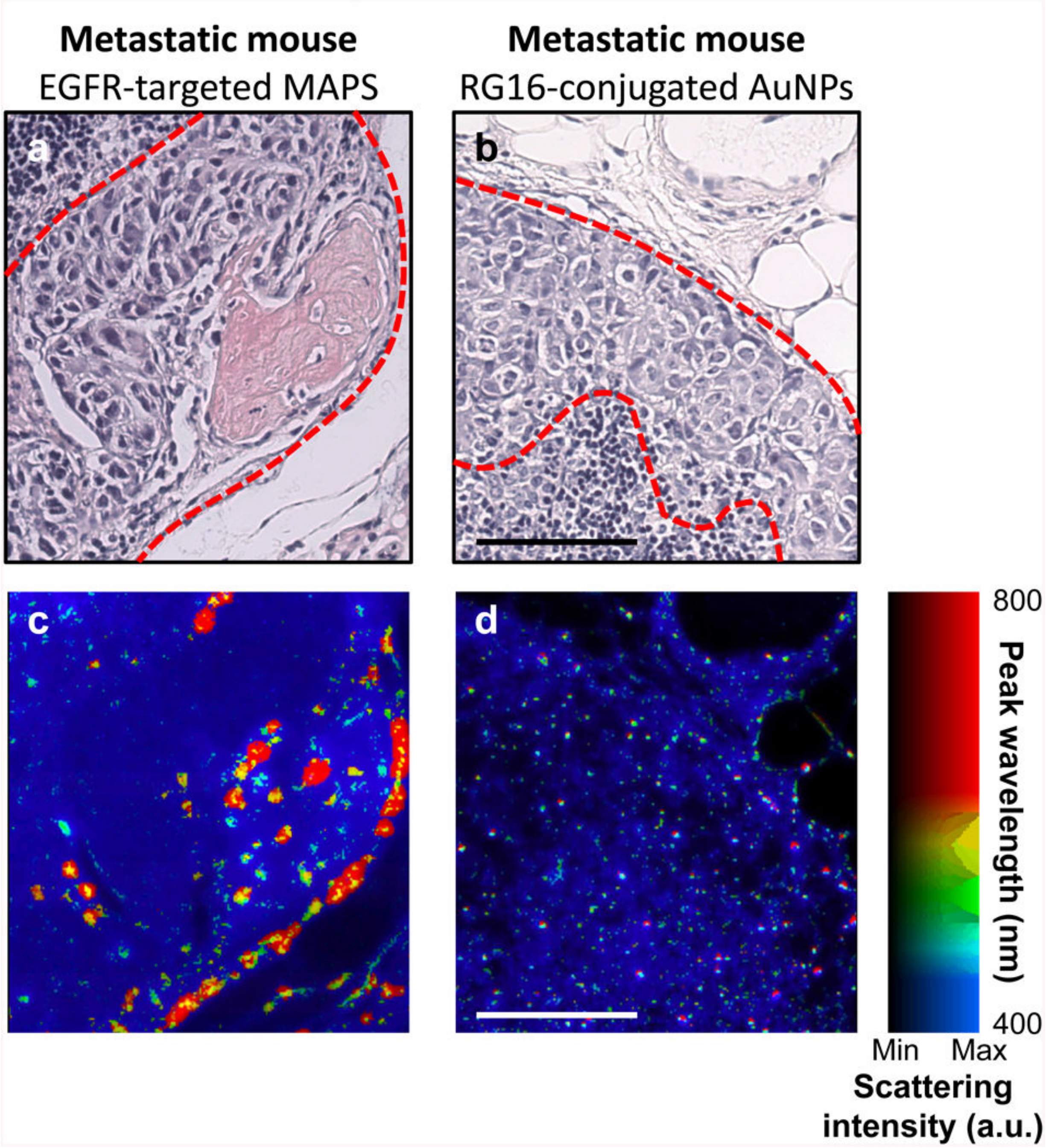

Fig. 7.

Optical hyperspectral microscopy of specific nanoparticle uptake and plasmon resonance coupling of MAPS. H&E stains of metastases (dashed red outline) in mice injected with either (**a**) EGFR-targeted MAPS or (**b**) RG16-targeted AuNPs. (**c** and **d**) Dark-field reflectance hyperspectral microscopy of adjacent tissue slices shows tumor cell uptake of EGFR-targeted MAPS and plasmon resonance coupling between the MAPS as evident from a strong red-NIR shift in their plasmon resonances with no plasmon resonance coupling observed after the injection of RG16-targeted AuNPs. The color in (c) and (d) indicates the wavelength of peak scattering intensity, while the brightness indicates the magnitude of scattering; the range of colors is depicted in the color bar. Scale bars are 100 μm.